Consequences of mode structure on plasma properties in electron cyclotron resonance sources

Ronald L. Kinder[a] and Mark J. Kushner[b]
Department of Electrical Engineering, University of Illinois, Urbana, Illinois 61801

(Received 29 January 1999; accepted 21 May 1999)

Low pressure (<50 mTorr) electron cyclotron resonance plasma sources are being developed for downstream etching and deposition and for production of radicals for surface treatment. The spatial coupling of microwave radiation to the plasma is a concern due to issues related to the uniformity of dissociation, electron heating, and ultimately process uniformity. To investigate these issues, a finite-difference-time-domain simulation for microwave injection and propagation has been developed, and has been incorporated as a module in the two-dimensional Hybrid Plasma Equipment Model. Results from parametric studies of N_2 plasmas suggest that obtaining uniform fluxes to the substrate may require a power deposition profile that is peaked off axis. An increase in power deposition tends to reinforce nonuniformities in the ion flux profile. At higher pressures (>10 mTorr) the sensitivity of the ion flux to the substrate to the angle of the magnetic field at the substrate decreases, while the uniformity of the ion flux improves. Due to the dependence of the collision frequency on electron temperature, losses from cross-field diffusion are enhanced in both the low and high pressure regimes. Results also suggest that there is an optimal pressure for maximizing both the magnitude of the ion flux to the substrate surface and its uniformity. © *1999 American Vacuum Society.* [S0734-2101(99)07305-4]

I. INTRODUCTION

Current requirements for plasma processing of microelectronics devices include the development of high plasma density sources that provide high deposition or etching rates, with improved process uniformity over large area wafers.[1–4] Due to their ability to obtain a high degree of ionization at low gas pressures, electron cyclotron resonance (ECR) sources are being developed for downstream etching and deposition and for production of radicals for surface treatment.[5–8] Efficient coupling of microwave radiation to the plasma in ECR reactors requires that the electron momentum transfer collision frequency be much smaller than the electron cyclotron frequency. Under these conditions, diffusion of electrons perpendicular to the magnetic field lines is small, thereby reducing losses to the wall. However, due to the low radial losses compared to the high longitudinal mobility of electrons, radial ionization profiles in the resonance zone are to some degree imprinted on the reactive fluxes reaching the substrate. As a result, the spatial coupling of microwave radiation to the plasma is a concern due to the resulting radial dependence of the ion sources.

The uniformity of the ion flux to the substrate has, in fact, been shown to strongly depend on the profile and location of the power deposition. Studies by Graves *et al.*[9] suggest that uniform fluxes to the substrate surface require a power deposition profile peaked off axis. Hidaka *et al.*[10] similarly showed that ECR plasma sources using a circular TE_{01} mode provided ion fluxes that have better uniformity over a larger area than that produced by conventional TE_{11} mode microwaves. In the case of the TE_{11} mode, the electric field has a maximum at the center of the waveguide. This likely produces larger rates of ionization on the axis of the plasma while diffusion losses are large at the edge.[11] On the other hand, the TE_{01} mode has a peak off axis, which may compensate for higher diffusion losses at the wall.

The finite-difference time-domain (FDTD) method has recently been used to investigate electromagnetic fields inside ECR sources. For example, Muta *et al.*[12] investigated microwave propagation in ECR plasmas using a one-dimensional simulation and compared the characteristics of their computed wave propagation with ray tracing. Tan and Grotjohn[13] developed a three-dimensional FDTD simulation of an unmagnetized plasma-loaded microwave cavity. The conductivity of the discharge was modeled by solving the electron momentum equation. More recently Gopinath and Grotjohn[14] developed a three-dimensional electromagnetic particle-in-cell (PIC) model to simulate a compact ECR source where the FDTD method was used to model the microwave fields.

To investigate coupling of TE_{0n} mode microwaves in ECR reactors, a FDTD simulation for microwave injection and propagation has been developed, and has been incorporated as a module in the two-dimensional Hybrid Plasma Equipment Model (HPEM).[15,16] Results from parametric studies of N_2 plasmas suggest that obtaining uniform fluxes to the substrate may require a power deposition profile that is peaked off axis. An increase in power deposition tends to reinforce any nonuniformities present in the ion flux profile. The model will be described in Sec. II, followed by a discussion of our results in Sec. III. Concluding remarks are in Sec. IV.

[a]Electronic mail: rkinder@uigela.ece.uiuc.edu
[b]Electronic mail: mjk@uiuc.edu

II. DESCRIPTION OF THE MODEL

The HPEM is a two-dimensional, plasma equipment model which consists of an electromagnetic module (EMM), an electron energy transport module (EETM), and a fluid kinetics simulation (FKS).[15,16] Electromagnetic fields and corresponding phases are calculated in the EMM. These fields are used in the EETM to solve the electron energy conservation equation or in a Monte Carlo simulation to generate sources for electron impact processes and electron transport coefficients. These parameters are transferred to the FKS where momentum and continuity equations are solved for all heavy particles. A drift diffusion formulation is used for electrons to enable an implicit solution of Poisson's equation for the electric potential. The species densities and electrostatic fields produced in the FKS are transferred to the EETM and the EMM. These modules are iterated until a converged solution is obtained.

In this work, a FDTD simulation integrates Maxwell's equations in the EMM to obtain the electromagnetic fields, $E(r,z,\phi)$ and $B(r,z,\phi)$, in the entire volume of the reactor. The implementation is cylindrical, two-dimensional on a rectilinear grid. Assuming charge neutrality and that the dielectric parameters μ, σ, and ϵ (permeability, conductivity, and permittivity, respectively) do not vary during the microwave cycle, the equations solved are

$$\frac{\partial E_\theta}{\partial t}=\frac{1}{\mu\epsilon}\left(\frac{\partial B_r}{\partial z}-\frac{\partial B_z}{\partial r}\right)-J_\theta, \tag{1a}$$

$$\frac{\partial B_r}{\partial t}=\frac{\partial E_\theta}{\partial z}, \tag{1b}$$

$$\frac{\partial B_z}{\partial t}=-\frac{1}{r}\frac{\partial (rE_\theta)}{\partial r}, \tag{1c}$$

where E_θ is the azimuthal component of the electric field, B_r and B_z are the radial and axial components of the magnetic field, $\bar{J}=\bar{\bar{\sigma}}\bar{E}$, $\bar{B}=\mu\bar{H}$, and $\bar{D}=\epsilon\bar{E}$. The conductivity tensor, $\bar{\bar{\sigma}}$, relates the current density to the electric field as

$$\begin{pmatrix}\tilde{J}_r\\ \tilde{J}_\theta\\ \tilde{J}_z\end{pmatrix}=\frac{qn_e}{\alpha(\alpha^2+B_r^2+B_z^2)}\times\begin{pmatrix}(\alpha^2+B_r^2) & B_z\alpha & B_rB_z\\ -B_z\alpha & \alpha^2 & B_r\alpha\\ B_rB_z & -B_r\alpha & (\alpha^2+B_z^2)\end{pmatrix}\begin{pmatrix}0\\ E_\theta\\ 0\end{pmatrix}, \tag{2}$$

where $\alpha=m/q(i\omega+\nu_m)$ for electron mass m, electric field frequency ω (rad/s), and electron momentum transfer collision frequency ν_m. To incorporate J_θ into our solution of Maxwell's equations, only the real component is considered,

$$J_\theta=\mathrm{Re}(\tilde{J}_\theta)=\frac{n_eq^2\nu_m}{2m_e}\left(\frac{1}{\nu_m^2+(\omega-\omega_c)^2}+\frac{1}{\nu_m^2+(\omega+\omega_c)^2}\right)E_\theta=\sigma_\perp E_\theta. \tag{3}$$

Doppler shifting of electrons into or out of resonance with the magnetic field is a significant phenomenon that can affect the shape and location of the conductivity. The consequences of Doppler shifting have been incorporated by using a modified velocity space averaged conductivity defined as

$$\bar{\sigma}_\perp=\frac{\iiint \sigma_\perp[\omega(\bar{v})]f(\bar{v})dv}{\iiint f(\bar{v})dv}, \tag{4}$$

and

$$\omega(\bar{v})=\omega_0\frac{1-(v_\parallel/c)}{\sqrt{1-(v_\parallel/c)^2}}, \tag{5}$$

where $f(\bar{v})$ is the electron velocity distribution function, ω_0 is the incident microwave frequency, $v_\parallel$ is the electron velocity parallel to the direction of propagation of the electromagnetic wave, and c is the speed of light. Numerical integration over velocity space is limited to $\pm 10\%$ the speed of light and is calculated by assuming a Boltzmann distribution.

The transverse electric (TE) fields injected into the reactor have $\bar{k}\cdot\bar{E}=0$, with components E_θ, B_r, and B_z as previously shown. The spatial locations of the components of $\bar{E}$ and $\bar{B}$ on the numerical mesh were chosen to provide centered spatial differencing. An alternating direction implicit (ADI) scheme with a $2\frac{1}{2}$-dimensional alternating grid was employed.[17] Azimuthal electric fields were calculated at meshpoints, while magnetic fields were calculated at locations shifted by half a mesh cell. A leapfrog scheme for time integration was used. The electric fields were calculated at time, t, and the magnetic fields were calculated at time, $t+\Delta t/2$. In doing so, the finite differencing representation of Eq. (1) is

$$\frac{E_\theta(i,j)^{t+\Delta t}-E_\theta(i,j)^t}{\Delta t}=\frac{1}{\mu\epsilon}\left(\frac{B_r(i,j+\frac{1}{2})-B_r(i,j-\frac{1}{2})}{\Delta z}-\frac{B_z(i+\frac{1}{2},j)-B_z(i-\frac{1}{2},j)}{\Delta r}\right)^{t+(\Delta t/2)}-\frac{\sigma_\perp}{\epsilon}E_\theta(i,j)^{t+\Delta t}, \tag{6a}$$

$$\frac{B_r(i,j+\frac{1}{2})^{t+(\Delta t/2)}-B_r(i,j+\frac{1}{2})^{t-(\Delta t/2)}}{\Delta t}=\frac{E_\theta(i,j+1)^t-E_\theta(i,j)^t}{\Delta z}, \tag{6b}$$

$$\frac{B_z(i+\frac{1}{2},j)^{t+(\Delta t/2)}-B_z(i+\frac{1}{2},j)^{t-(\Delta t/2)}}{\Delta t}$$

$$=\frac{[r(i+1,j)E_\theta(i+1,j)^t-r(i,j)E_\theta(i,j)^t]}{[r(i,j)+(\Delta r/2)]\Delta r}, \tag{6c}$$

where (i,j) corresponds to mesh points (r,z), Δr and Δz are the mesh spacings in the r and z directions, and Δt is the integration time step. The Courant condition on the allowed time step is given by

$$\left(\frac{1}{\Delta r^2}+\frac{1}{\Delta z^2}\right)^{(1/2)}\frac{1}{c}>\Delta t, \tag{7}$$

where c is the speed of light.

When time domain electromagnetic fields are obtained using finite-difference techniques in an unbounded space, there must ultimately be a method of limiting the domain in which the field is computed. This is achieved here by using absorbing boundary conditions at chosen edges of the numerical mesh. Due to the nature of the ADI scheme, boundary conditions which use constant gradients for electromagnetic fields cause spurious reflections of the incident waves. To remove these unwanted reflections a linearized first order wave equation was imposed as a boundary condition to simulate empty space,

$$\frac{\partial E_\theta^{n+1}(i,j)}{\partial z}+\frac{\partial E_\theta^{n}(i,j)}{\partial z}=\frac{1}{c}\left(\frac{\partial E_\theta(i,j)}{\partial t}+\frac{\partial E_\theta(i,j-1)}{\partial t}\right). \tag{8}$$

The system of interest uses circular TE_{0n} microwave mode fields injected along the axis of a cylindrically symmetric downstream reactor to excite the plasma. The complex electric and magnetic field components for the injected circular TE_{mn} mode waves are

$$\mathcal{E}_\theta=A_{mn}\frac{\beta_r}{\epsilon}J_m'(\beta_r r)[C_2\cos(m\phi)$$
$$+D_2\sin(m\phi)]\exp(-j\beta_r z), \tag{9a}$$

$$\mathcal{H}_r=-A_{mn}\frac{\beta_z\beta_r}{\omega\mu\epsilon}J_m'(\beta_r r)[C_2\cos(m\phi)$$
$$+D_2\sin(m\phi)]\exp(-j\beta_r z), \tag{9b}$$

$$\mathcal{H}_z=-jA_{mn}\frac{\beta_r^2}{\omega\mu\epsilon}J_m(\beta_r r)[C_2\cos(m\phi)$$
$$+D_2\sin(m\phi)]\exp(-j\beta_r z), \tag{9c}$$

where $\mathcal{E}_\theta$, $\mathcal{H}_r$, and $\mathcal{H}_z$ are the complex azimuthal electric field, radial magnetic field intensity, and axial magnetic field intensity, respectively, and $J(\beta_r r)$ and $J'(\beta_r r)$ are the Bessel functions and their derivatives. The amplitude of these fields (with their appropriate phases) were impressed as boundary conditions at the mouth of the waveguide at the entrance of our reactor.

For purposes of quantifying the uniformity of the ion flux, Φ, to the substrate, the uniformity parameter is defined as

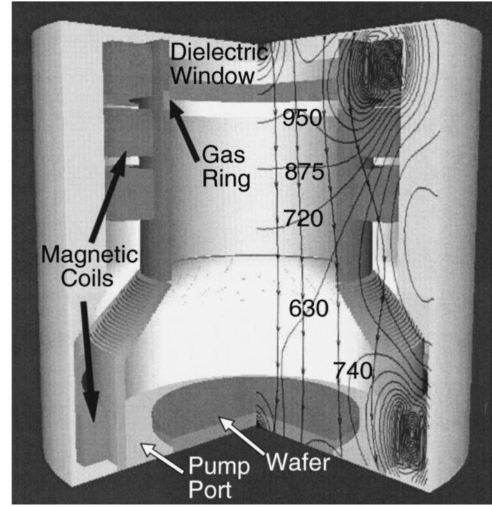

FIG. 1. Geometry for the electron cyclotron resonance simulation. The magnetic field magnitude in (gauss) and the magnetic flux field lines are shown on the right side.

$$\eta=1-\frac{|\Phi_{\mathrm{Peak}}-\langle\Phi\rangle_{\mathrm{Average}}|}{\langle\Phi\rangle_{\mathrm{Average}}}, \tag{10}$$

where Φ_{Peak} is the peak flux on the wafer and $\langle\Phi\rangle_{\mathrm{Average}}$ is the area weighted average across the wafer. Larger η is more uniform.

III. ECR EXCITATION WITH TE_{0n} MODES

The reactor we investigated is schematically shown in Fig. 1. The waveguide which injects the TE_{0n} field terminates at the top of the reactor above the microwave window. Gases are injected into the reactor through a ring nozzle located near the microwave window and are exhausted at the bottom of the reactor through an annular pump port. Nitrogen is the feedstock gas at pressures of 0.5–50 mTorr, flow rates of 5–20 sccm (resulting in residence times of a few milliseconds), and power deposition of 500–1500 W. The collisional processes in the model are listed in Table I and include ionization, excitation, and momentum transfer collisions between electrons and neutral particles, Coulomb collisions between electrons and ions, charge exchange collisions between ions and neutral particles, and momentum transfer collisions among neutral particles. Electron impact reactions with molecular nitrogen include excitation up to the eighth vibrational state (lumped into a single effective vibrational state) and up to the third electronic state of N_2 (lumped into a single effective electronic state).

The base case was N_2 at 1 mTorr, 10 sccm, and 750 W. The circularly transverse electric fields, operating at 2 GHz, were used to sustain the plasma are injected at the top of the reactor through the waveguide antenna. The wave propagates through the dielectric window and into the processing chamber. The static magnetic field, generated by a direct current solenoid, is designed to produce a resonance zone in the throat of the chamber and is shown on the right side in Fig. 1. The top set of magnetic coils is used to determine the location of the resonance. The coil at the bottom of the re-

TABLE I. Gas phase reactions for N_2.

Reaction[a]	Rate coefficient[b]	Reference
$e+N_2 \rightarrow e+N_2(X\ ^1\Sigma_g^+, v=1-8)$	c	22
$e+N_2 \rightarrow e+N_2(A\ ^3\Sigma_u^+, B\ ^3\Pi_g, B^{1\ 3}\Sigma_u^-, a^{1\ 3}\Sigma_u^-, C\ ^3\Pi_u)$	c	22
$e+N_2 \rightarrow e+N+N$	c	22
$e+N_2 \rightarrow 2e+N_2^+$	c	22
$e+N_2(v) \rightarrow e+N_2$	c	c
$e+N_2(v) \rightarrow e+N_2^*$	c	22[d]
$e+N_2(v) \rightarrow 2e+N_2^+$	c	22[d]
$e+N_2^* \rightarrow e+N_2(v)$	c	22[d]
$e+N_2^* \rightarrow e+N_2$	c	c
$e+N_2^* \rightarrow 2e+N_2^+$	c	23
$e+N_2^+ \rightarrow N^*+N$	1×10^{-7}	24
$e+N \rightarrow e+N^*$	c	25
$e+N \rightarrow 2e+N^+$	c	26
$e+N^* \rightarrow e+N$	c	c
$e+N^* \rightarrow e+N^+$	b	23
$N_2^*+N_2 \rightarrow 2N_2$	1.9×10^{-13}	27
$N_2^*+N \rightarrow N_2+N$	1×10^{-13}	d
$N_2^*+N^* \rightarrow N_2+N$	1×10^{-13}	d
$N^*+N_2 \rightarrow N+N_2$	2×10^{-14}	d
$N^*+N+M \rightarrow N_2^*+M$	2×10^{-32}	28[d]
$2N+M \rightarrow N_2^*+M$	1×10^{-32}	28[d]
$2N+M \rightarrow N_2+M$	1×10^{-32}	28
$2N_2^* \rightarrow N_2^*+N_2$	1.36×10^{-9}	29
$N_2(v)+N_2 \rightarrow 2N_2$	1×10^{-13}	d
$N_2(v)+N \rightarrow N_2+N$	1×10^{-14}	d
$N_2(v)+N^* \rightarrow N_2+N$	1×10^{-14}	d
$N_2^++N \rightarrow N_2+N^+$	5×10^{-12}	30
$N_2^++N^* \rightarrow N_2+N^+$	1×10^{-10}	d
$N_2^++N_2 \rightarrow N_2+N_2^+$	5×10^{-10}	31
$N_2^++N_2^* \rightarrow N_2+N_2^+$	1×10^{-9}	d
$N_2^++N_2(v) \rightarrow N_2+N_2^+$	1×10^{-9}	d
$N^++N \rightarrow N+N^+$	1×10^{-9}	d
$N^++N^* \rightarrow N+N^+$	1×10^{-9}	d
$N^++N_2^* \rightarrow N_2^++N$	1×10^{-9}	d

[a]In the FKS, all vibrational excitations of $N_2(X\ ^1\Sigma_g^+)$ are lumped into $N_2(v)$, which is effectively $N_2(X\ ^1\Sigma_g^+\ v=1)$, and all electronic excitations of $N_2(X\ ^1\Sigma_g^+)$ are lumped into N_2^*, which is effectively $N_2(A\ ^3\Sigma_u^+)$. N denotes $N(^4S^0)$, N* denotes $N(^2D^0)$.
[b]Rate coefficients are calculated from the electron energy distribution obtained from the EETM.
[c]Detailed balance.
[d]Estimated.

actor (the ''subcoil'') is used to tailor the divergence of the magnetic field in the vicinity of the wafer, and so controls the flux profiles to the wafer. The conductivity and the power deposition for the base case are shown in Fig. 2(a). The primary resonance occurs in the upper region of the reactor where $B=714$ G. There is also a secondary resonance located downstream that occurs when the subcoil is employed. The conductivity shown on the left side of Fig. 2(a) is a maximum in the resonant zone with a peak value of $0.035\ \Omega^{-1}\ \mathrm{cm}^{-1}$ falling off by a factor of 10^4 in a 2.2 cm axial range. The conductivity has a full width at half maximum ($\Delta\omega_{ce}=6.5$G) corresponding to approximately twice the electron collision frequency, $2\nu_m$.

The power deposition, shown on the right side of Fig. 2(a), mirrors the conductivity in the axial direction. The power deposition reflects the profile of the azimuthal electric field along the radial direction since it has a node on axis and peaks at about half the radius. Power deposition occurs predominantly within the resonance zone where peak values are $15.2\ \mathrm{W\,cm^{-3}}$ and falls off by a factor of 10^4 in a 2.6 cm axial distance downstream. The electric field is large (~200 V/cm) upstream of the resonance zone, as shown on the left side of Fig. 2(b). Even though the conductivity is small upstream, there is non-negligible power deposition which constitutes about 20% of the total, a component of which is due to Doppler shifting of the resonance zone. The electric field is not totally absorbed in the resonance zone. Some amplitude is either transmitted through or diffracts around the resonance zone allowing some small amount of power deposition at the resonance near the subcoil.

Electron temperatures in ECR sources are typically higher than those obtained in inductively coupled plasma (ICP) devices.[18] Electron temperatures can exceed 8 eV at pressures <0.5 mTorr. Electron temperatures in the resonance zone reflect radial power deposition distributions and have a peak value of 7.1 eV, as shown on the right side of Fig. 2(b). This results in an off axis electron source function as shown on the left side of Fig. 2(c). In the steady state, the plasma generation by ionization is in balance with losses due to transport. The solenoidal magnetic field minimizes radial diffusion losses and electron thermal conduction. Diffusion and thermal conduction mainly occur along the magnetic field lines in the axial direction thereby allowing the radial electron temperature distribution and electron source function to maintain their profile far into the downstream region. The resulting electron densities are shown on the right side of Fig. 2(c). The electron density is maximum in the resonance zone with a value of $1.58\times10^{11}\ \mathrm{cm}^{-3}$. For these operating conditions, the radial distribution of densities tends to reflect their radial sources due to the strong radial confinement of electrons by the magnetic field. As a consequence of a small amount of power deposition that occurs near the subcoil, there is a local peak in the electron density.

Simulation results were benchmarked against experimental results obtained by Uhm *et al.*[19] Comparisons of the electron temperature and the electron density in the resonance region as a function of pressure are compared with experimental data in Fig. 3 for an argon plasma at 700 W and 10 sccm. The calculation systematically agrees with the experiments, with a shift of a few Torr. We attribute this shift to rarefraction of the gas in the resonance zone, which is not accounted for in the calculations. The increase in electron temperature in the low pressure regime is due to an increase in efficiency for absorbing microwave energy, a decrease in collisional cooling, and an increase in axial losses. In the low pressure regime, ion diffusion along the axial magnetic field lines dominates the losses, and the density decreases. As the pressure is increased, radial losses become increasingly more significant thereby producing an optimal pressure for maximum plasma density.

Parametric studies show that the spatially dependent plasma properties are a sensitive function of pressure. Ion

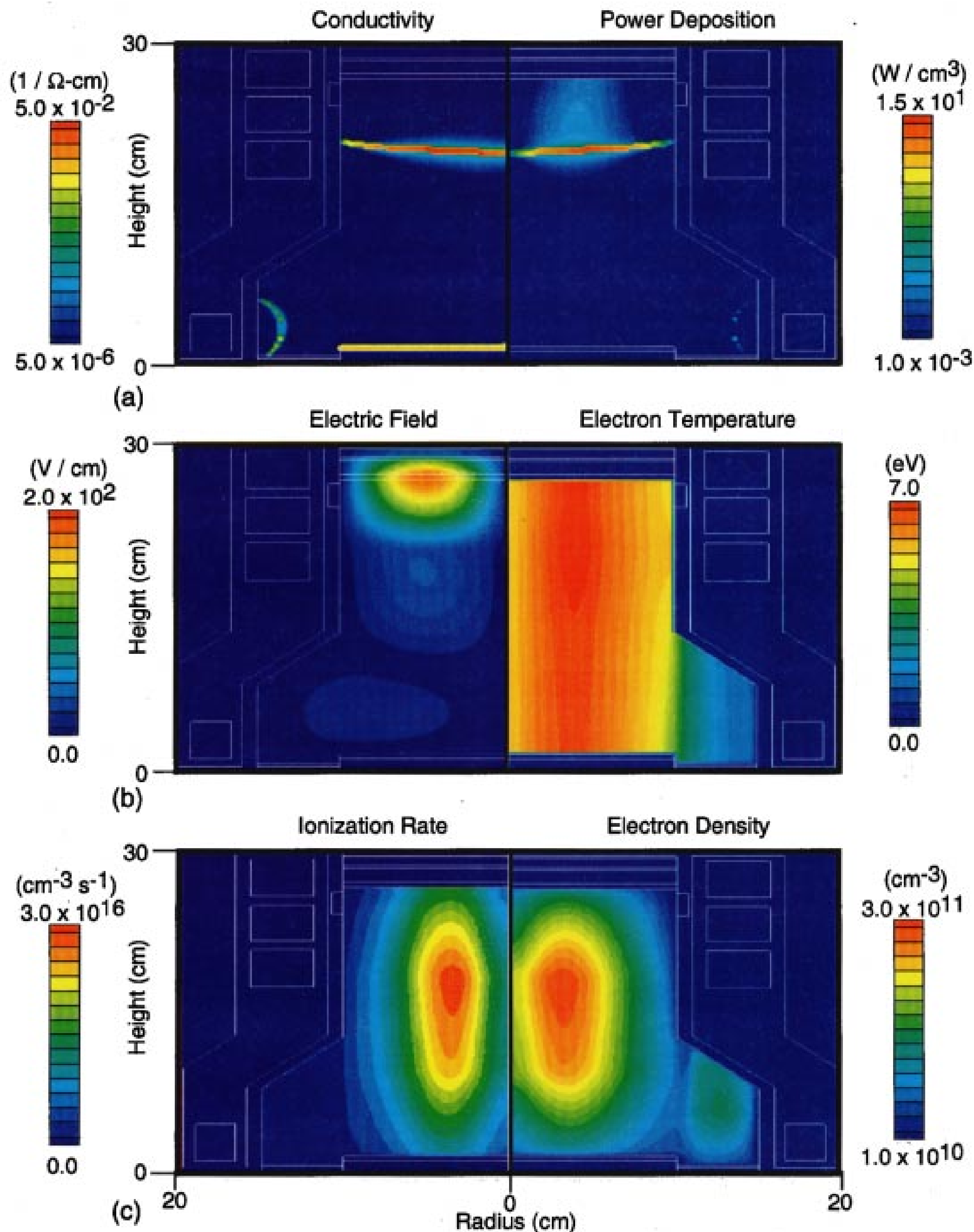

FIG. 2. Plasma parameters for the base case using TE_{01} excitation. (a) Plasma conductivity (the wafer conductivity is also shown), and power deposition (b) azimuthal electric field magnitude and electron temperature and (c) ionization rate and electron density.

densities as a function of position for pressures of 0.5, 1.0, and 10 mTorr are shown in Fig. 4 and have peak densities of $2-3\times10^{11}\,\mathrm{cm}^{-3}$. As the pressure is decreased below 2 mTorr, there is a shift in the peak electron (and ion) density towards the center of the reactor. At 10 mTorr the plasma is peaked at the location of peak power deposition and becomes increasingly more uniform towards the substrate due to cross field diffusion. At 1 mTorr, the plasma density is similarly peaked near the location of peak power deposition, although with a shift toward smaller radii. The density maintains its off axis peak far into the downstream region. At 0.5 mTorr, the density has shifted and is now peaked near the center of the chamber. The ion flux to the substrate, shown in Fig. 5(a) reflects the spatial dependence of the ion density with its shift towards the center of the reactor at pressures below 1 mTorr. The radially averaged ion flux and ion flux uniformity are shown in Fig. 5(b). At 10 mTorr, the ion flux peaks near a radius of 5 cm at a value of $8.5\times10^{15}\,\mathrm{cm}^{-2}\,\mathrm{s}^{-1}$, with a uniformity of η=78%. As the pressure decreases below 1 mTorr, the peak in the ion flux shifts towards the center of the reactor and the peak in the ion flux increases to $5.0\times10^{16}\,\mathrm{cm}^{-2}\,\mathrm{s}^{-1}$ at 0.75 mTorr. The uniformity, however,

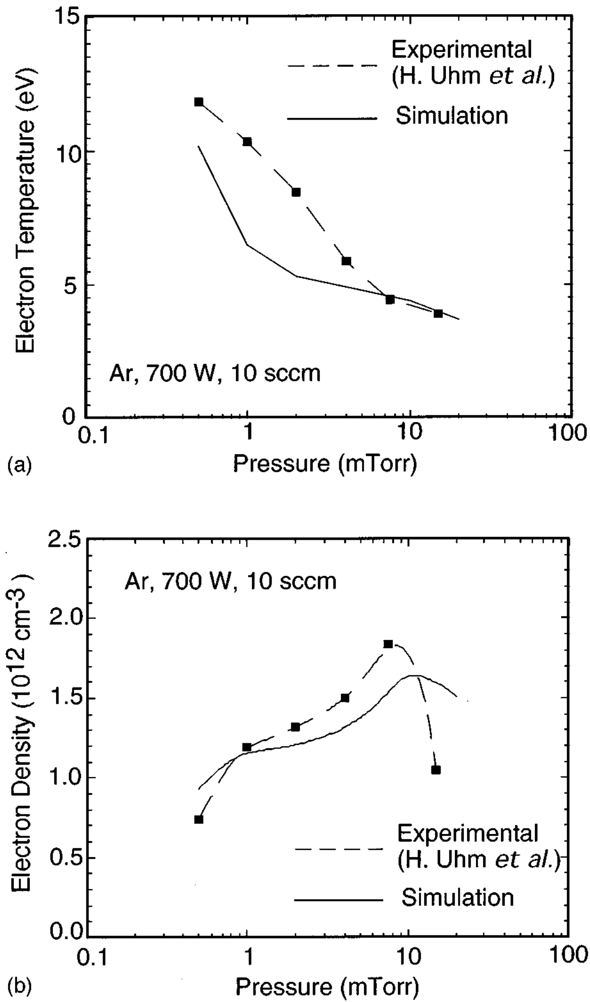

FIG. 3. Experimental (Ref. 19) and computed values of (a) electron temperature and (b) electron density in the resonance zone of an ECR processing tool operating in argon with varying pressures.

falls to η=45%. At 0.5 mTorr the ion flux peaks at the center and has having a value of $2.75\times10^{15}\,\mathrm{cm}^{-2}\,\mathrm{s}^{-1}$, while the uniformity improves to η=60%. Note that at the pressure at which the average ion flux is maximum (0.75 mTorr) uniformity is a minimum indicating that there will be a trade-off with respect to maximizing ion flux and optimizing uniformity.

The decrease in ion flux and increase in uniformity is to some degree expected in the high pressure regime. For these operating pressures, the cyclotron frequency is much larger than the momentum transfer collision frequency. Hence the longitudinal diffusion coefficient scales inversely to the momentum transfer collision frequency, while the transverse diffusion coefficient scales with the momentum transfer collision frequency. The off axis ion source is smoothed by transverse diffusion, thereby improving flux uniformity, while the increased radial losses diminish the magnitude of the flux. The lower electron temperature also increases the proportion of power that is dissipated in nonionizing electron collisions, thereby decreasing the ion density for constant power deposition.

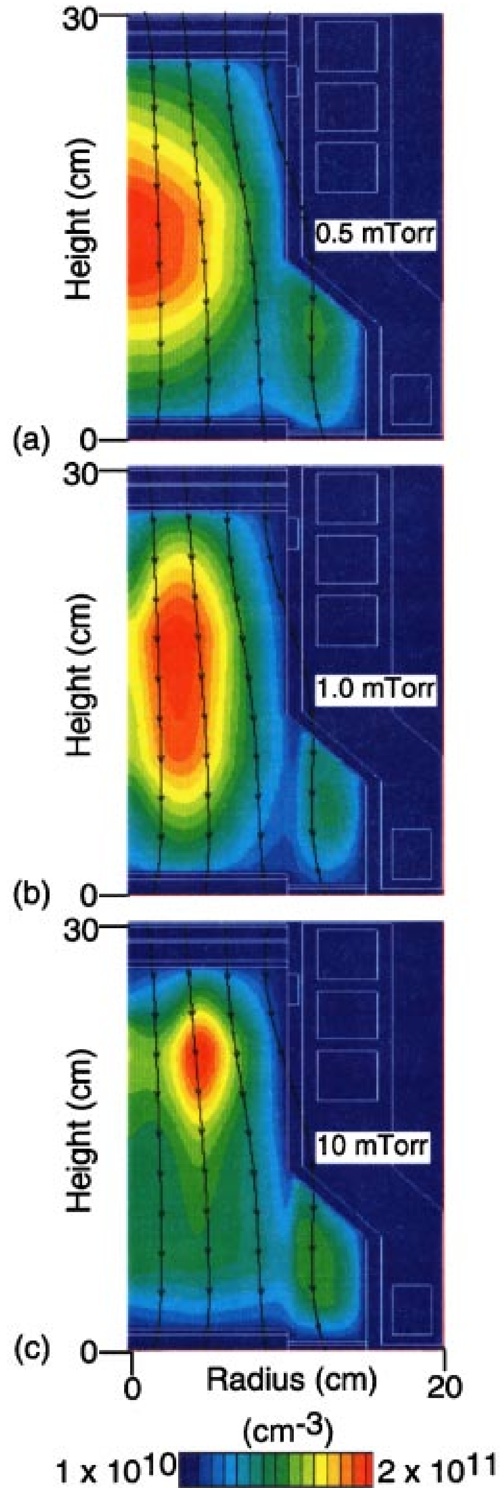

FIG. 4. Electron density at (a) 0.5, (b) 1.0, and (c) 10.0 mTorr for a TE_{01} mode field. There is a counter intuitive shift of the peak in the plasma density to the center of the reactor at low pressure.

In the low pressure regime, the average ion flux decreases with decreasing pressure, while the uniformity increases. More significantly, the peak in the plasma density profile shifts toward the center of the reactor. This trend suggests that there is an increase in diffusion perpendicular to the magnetic field lines enabling the electron density to take on a

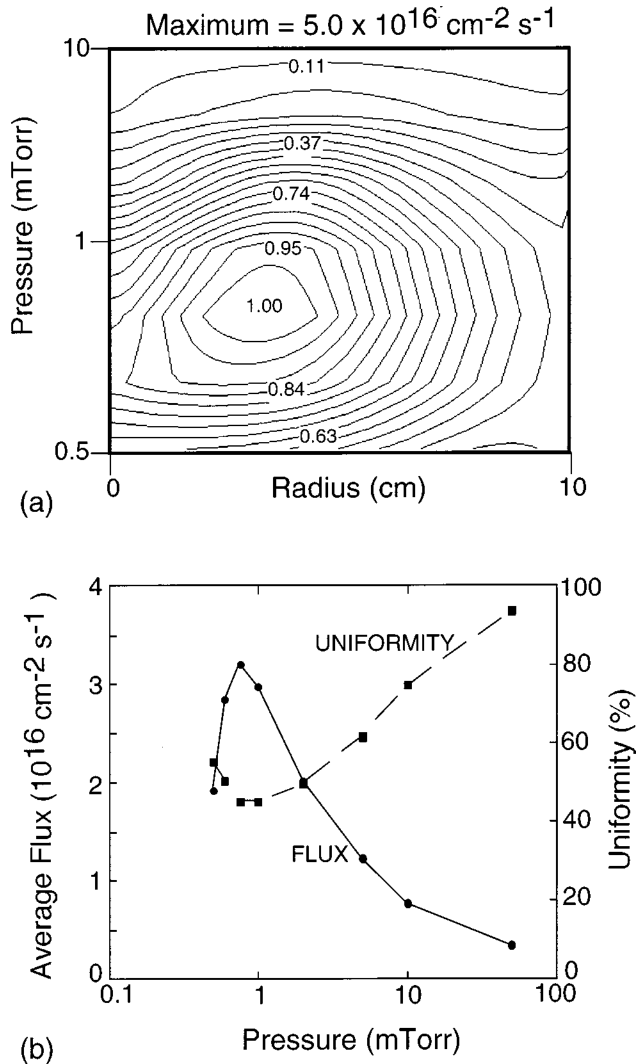

FIG. 5. Ion flux parameters as a function of pressure. (a) Ion flux as a function of radius for varying chamber pressures. The ion flux profile follows the shift in the electron (ion) density profile. (b) Radially averaged ion flux and uniformity of the ion flux to the substrate as a function of pressure.

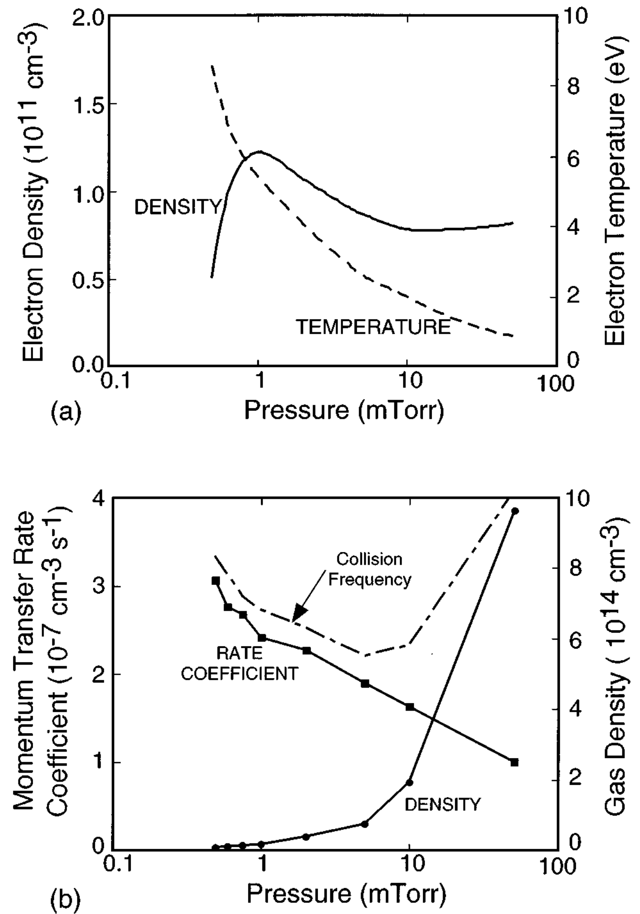

FIG. 6. Plasma parameters as a function of pressure for the N_2 discharge. (a) Average electron density and electron temperature for varying pressures. (b) Average electron momentum transfer rate coefficient, electron momentum transfer collision frequency, and neutral gas density as a function of gas pressure. The collision frequency is the product of the rate coefficient and the neutral gas density and is plotted in relative units.

diffusion dominated profile. Such a trend is counterintuitive, since transport across the magnetic field lines decreases with decreasing collision frequency and, at lower pressures, the collision frequency is expected to decrease.

This increase in collision frequency at lower pressures which produces enhanced diffusion can be attributed to an increase in the electron temperature. For reference, the average electron density and electron temperature as a function of gas pressure are shown in Fig. 6(a). The reactor average electron density peaks around 1 mTorr at a value of 1.25 $\times 10^{11}$ cm^3. As the pressure is decreased, the average plasma density falls to a value of 5.0×10^{10} cm^{-3} at 0.5 mTorr. As the pressure is increased above 1 mTorr, the average plasma density falls off, but at a more gradual rate, to a value of 8.0×10^{10} cm^{-3} at 50 mTorr. The average electron temperature increases slowly at higher pressures, from 1 eV at 50 mTorr to 3 eV at 2 mTorr, and increases at a faster rate below 2 mTorr, reaching a value of ~8 eV at 0.5 mTorr. Such trends agree with results obtained by Wu *et al.*[20] who used a two-dimensional simulation and a global conservation model. This increase in electron temperature is due to a decrease in collisional cooling and larger axial diffusion losses which require a higher ionization rate to compensate for.

The electron momentum transfer rate coefficient, the electron momentum transfer collision frequency, and neutral gas density as a function of gas pressure are shown in Fig. 6(b). Note that the momentum transfer rate coefficient increases with increasing electron temperature, so the rate coefficient for momentum transfer also increases with decreasing pressure. Similarly, as the pressure increases, the electron temperature decreases thereby decreasing the rate coefficient, while the gas density increases. The rate of increase in the rate coefficient for momentum transfer exceeds the decrease in gas density in the low pressure regime while the increase in gas density exceeds the decrease in the rate coefficient in the high pressure regime. Therefore the electron momentum

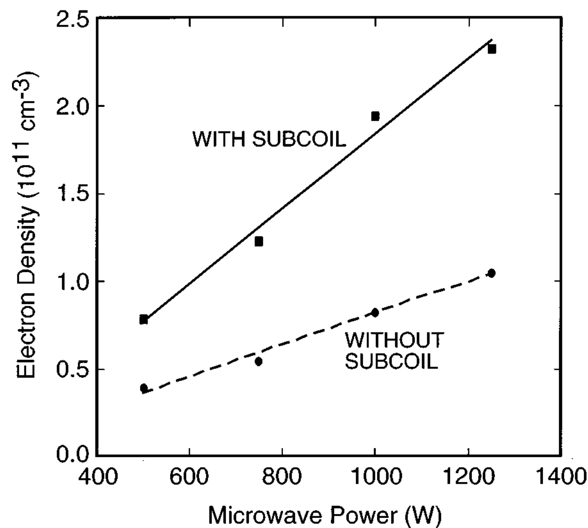

FIG. 7. Average reactor electron density with and without activation of the magnetic subcoil as a function of power. Use of the subcoil increases both the plasma density and ionization efficiency.

transfer collision frequency, which is the product of the momentum transfer rate coefficient and the gas density, actually increases in both the low and high pressure regimes. This increase of the collision frequency in the low pressure regime produces enhanced electron diffusion across the magnetic field lines and hence improves uniformity while increasing diffusion losses and decreasing density.

The bottom coil can be used to tailor the magnetic field in the vicinity of the substrate and hence can influence the flux of charged species to the substrate. For example, by producing a solenoidal magnetic field, radial transport losses are significantly reduced. These trends are demonstrated in Fig. 7, where the average reactor electron densities as a function of power with and without activation of the subcoil are shown. The electron density is higher with the subcoil activated due to the more confining solenoidal magnetic field which prevents magnetic field lines from intersecting the walls, thereby reducing transport losses. The power efficiency, defined as the average electron density divided by the total power deposition, is also greater. For example, with the subcoil the slope ionization efficiency is 2.2×10^8 cm^{-3}/W, whereas without the subcoil, the efficiency is 0.9×10^8 cm^{-3}/W.

The solenoidal magnetic field obtained when activating the subcoil results in the plasma density having the same radial profile near the substrate as that produced in the resonance zone. For example, the consequences of activating the subcoil on the ion flux to the substrate are shown in Fig. 8. In general the ion flux increases with increasing power with activation of the subcoil, however the uniformity decreases (η=86% at 500 W and η=69% at 1000 W). With activation of the subcoil any nonuniformities imprinted in the resonance zone are enhanced as the power is increased. Without activating the subcoil, the ion flux is lower, but the uniformity is improved and is a weaker function of power deposition (η=95% at 500 W and η=83% at 1000 W).

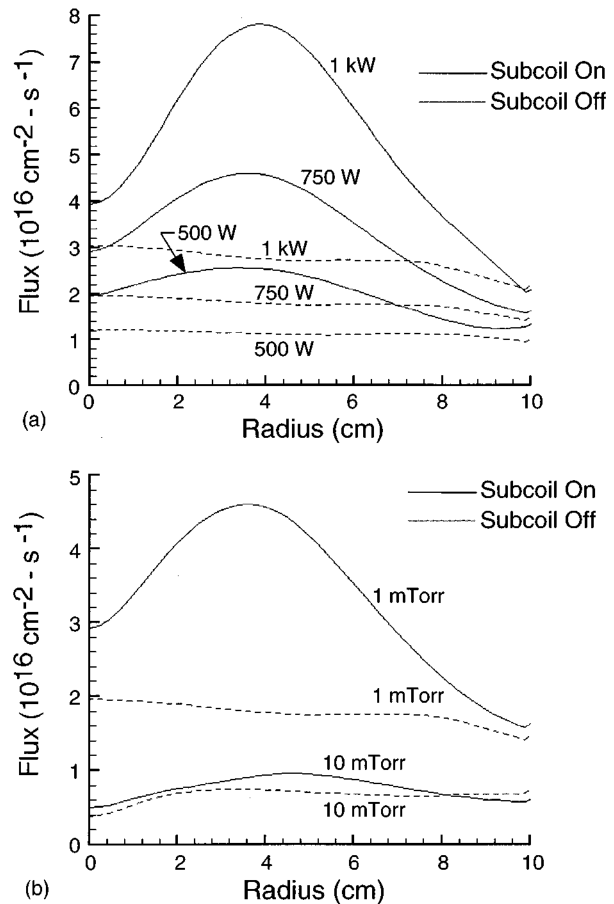

FIG. 8. Radial ion flux profile to the substrate with and without activation of the magnetic subcoil as a function of (a) power and (b) pressure. The dashed lines are for fluxes with the subcoil off.

Higher order circular $TE_{0,n}$ modes have additional off axis peaks in the electric field, depending on the harmonic used, and therefore additional peaks in the off axis power deposition peaks. Experimental observations[21] have shown that the uniformity of the ion flux to the substrate improves with increasing mode number. For example, the azimuthal electric field component of the TE_{02} mode has an off axis node that produces two peaks in the field amplitude with the magnitude of the outer peak being smaller than that of the inner peak. Simulations were performed for the standard cases using a TE_{02} mode. The resulting power deposition profile, shown on the left side of Fig. 9(a), reflects the field intensity of the azimuthal electric field component with two separate regions of power deposition. The peak power deposition in the outer peak is roughly half that of the inner peak as shown in Fig. 9(b). As a result, the electron temperature is more uniform as a function of the radius. Enhanced diffusion along the magnetic field lines allows the radial electron temperature distribution to maintain its profile far into the downstream region. As a consequence, the electron density peaks closer to the axis and is in general more uniform than when using the TE_{01} mode.

Ion flux profiles tend to reflect the off axis peaks in ionization rates and plasma densities, and tying of the flux to

magnetic field lines. The effects of subcoil activation on ion flux to the substrate are shown in Fig. 10(a) for the TE_{02} mode. The ion flux profile with the subcoil off reflects only the inner peak in the power deposition for the TE_{02} mode. The ion flux originating from the outer peak is lost to either radial diffusion or drift along magnetic field lines that intersect the walls. Activation of the subcoil reduces radial losses and enhances the ion flux uniformity. The peak ion fluxes to the wafer for higher order modes are higher than those produced by the lower mode fields, with or without activation of the subcoil. However, since the position of the higher TE_{02} peak is at a smaller radius ($r = 1.8$ cm) than the peak value of the lower TE_{01} peak ($r = 3.9$ cm), the overall average ion flux to the substrate is higher for the lower mode, as is shown in Fig. 10(b).

IV. CONCLUDING REMARKS

A finite-difference-time-domain simulation for microwave injection and propagation has been developed to examine the spatial coupling of microwave radiation to the plasma in an electron cyclotron resonance reactor and its effect on uniformity. The FDTD simulation was incorporated as a module in the two-dimensional Hybrid Plasma Equipment Model. Plasma dynamics were coupled to the electromagnetic fields through a tensor form of Ohm's law. Power deposition calculated in the FDTD module is then used in solving the electron energy equation. Consequences of mode structure, magnetic field configuration, and operating conditions on plasma parameters and fluxes to the substrate in ECR sources for materials processing were examined with this model.

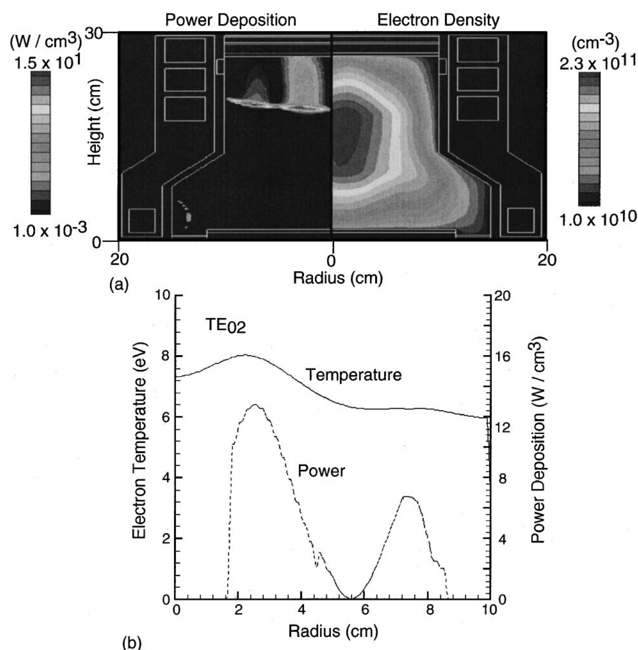

FIG. 9. Plasma parameters for the base case condition (750 W, N_2, 1.0 mTorr) for excitation with the TE_{02} mode. (a) Power deposition and electron density. (b) Radial profiles of the electron temperature and power deposition in the resonance zone ($z = 20$ cm).

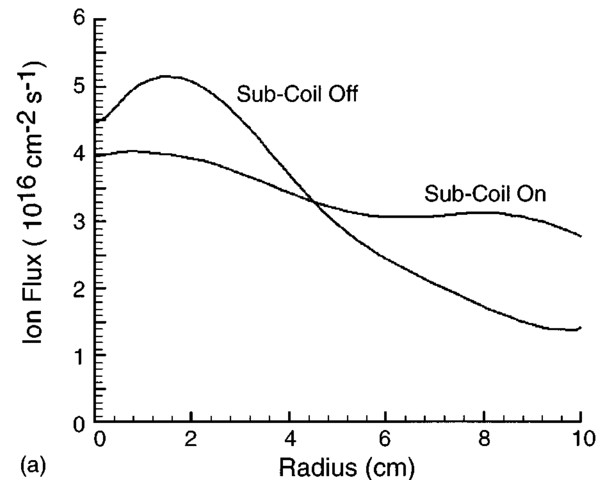

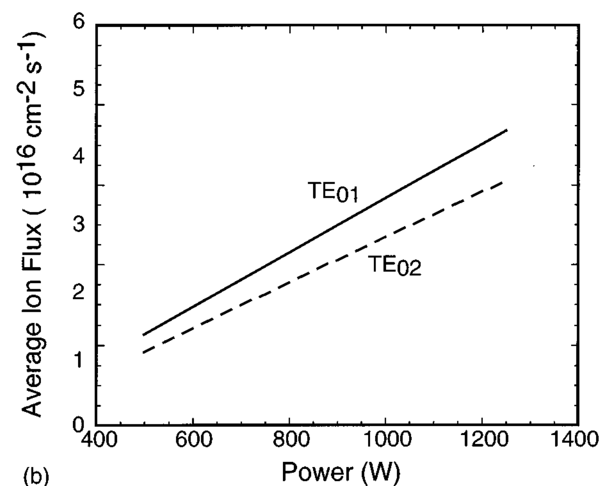

FIG. 10. (a) Radial ion flux to the substrate for a TE_{02} mode field with and without activation of the subcoil in a N_2 discharge operating at 1.0 mTorr and 750 W. (b) Average ion flux to the substrate for the TE_{01} and TE_{02} modes as a function of power in the N_2 discharge at 750 W.

The results for varying magnetic coil configurations showed that when operating with the subcoil the ion flux to the substrate generally reflected the ion density profiles in the resonance zone. An increase in power leads to the enhancement of nonuniformities in the flux profile. At higher pressures the sensitivity of the ion flux to activation of the subcoil is decreased and the uniformity of the ion flux is increased. For these particular conditions, cross field diffusion losses are enhanced in the low pressure regimes due to an increase in the electron temperature and collision frequency. The results suggest that there is an optimal pressure for charged particle confinement, maximizing ion flux to the substrate surface, and ion flux uniformity.

ACKNOWLEDGMENTS

This work was supported by the Semiconductor Research Corp., DARPA/AFOSR through the North Carolina State University Multidisciplanary University Research Initiative, LAM Research Corp., and Applied Materials Inc.

[1]J. L. Cecchi, in *Handbook of Plasma Processing Technology*, edited by S. M. Rossnagel, J. J. Cuomo, and W. D. Westwood (Noyes, Park Ridge, NJ, 1990), Chap. 2.
[2]N. Blayo *et al.*, J. Vac. Sci. Technol. B **12**, 1340 (1994).
[3]W. Z. Collison, T. Q. Ni, and M. S. Barnes, J. Vac. Sci. Technol. A **16**, 100 (1998).
[4]I. Ghanashev, M. Nagatsu, S. Morita, and H. Sugai, J. Vac. Sci. Technol. A **16**, 1537 (1998).
[5]J. Asmussen, J. Vac. Sci. Technol. A **7**, 883 (1989).
[6]J. E. Stevens, Y. C. Huang, R. L. Jarecki, and J. L. Cecchi, J. Vac. Sci. Technol. A **10**, 1270 (1992).
[7]T. A. Grotjohn, W. Tan, V. Gopinath, A. K. Srivastava, and J. Asmussen, Rev. Sci. Instrum. **65**, 1762 (1994).
[8]M. Meyyappan and T. R. Govindan, IEEE Trans. Plasma Sci. **23**, 623 (1995).
[9]D. B. Graves, H. Wu, and R. K. Porteous, Jpn. J. Appl. Phys., Part 1 **32**, 2999 (1993).
[10]R. Hidaka, T. Yamaguchi, N. Hirotsu, T. Ohshima, R. Koga, M. Tanaka, and Y. Kawai, Jpn. J. Appl. Phys., Part 1 **32**, 174 (1993).
[11]H. Kim, Y. Tuchihashi, K. Matsuo, K. Muraoka, and M. Akazaki, Trans. Inst. Electr. Eng. Jpn., Part A **109**, 149 (1989).
[12]H. Muta, T. Sakoda, Y. Ueda, and Y. Kawai, Jpn. J. Appl. Phys., Part 1 **36**, 872 (1997).
[13]W. Tan and T. A. Grotjohn, J. Vac. Sci. Technol. A **12**, 1216 (1994).
[14]V. P. Gopinath and T. A. Grotjohn, IEEE Trans. Plasma Sci. **23**, 602 (1995).
[15]M. J. Grapperhaus and M. J. Kushner, J. Appl. Phys. **81**, 569 (1997).
[16]S. Rauf and M. J. Kushner, J. Appl. Phys. **81**, 5966 (1997).
[17]C. K. Birdsall and A. B. Langdon, *Plasma Physics via Computer Simulation* (Hilger, New York, 1991).
[18]C. A. Outten, J. C. Barbour, and W. R. Wampler, J. Vac. Sci. Technol. A **9**, 717 (1991).
[19]H. S. Uhm, P. H. Lee, Y. I. Kim, J. H. Kim, and H. Y. Chang, IEEE Trans. Plasma Sci. **23**, 628 (1995).
[20]H. Wu, D. B. Graves, and R. K. Porteous, Plasma Sources Sci. Technol. **4**, 22 (1995).
[21]Y. Ueda and Y. Kawai, Appl. Phys. Lett. **71**, 2100 (1997).
[22]A. V. Phelps and L. C. Pichford, JILA Datacenter Report 26, 1985.
[23]L. Vriens, Phys. Lett. **8**, 260 (1964).
[24]J. B. A. Mitchell, Phys. Reports **186**, 215 (1990).
[25]R. J. W. Henry, P. G. Burke, and A. L. Sinfailam, Phys. Rev. **178**, 218 (1969).
[26]A. C. H. Smith, Phys. Rev. **127** 1647 (1962).
[27]L. G. Piper, J. Chem. Phys. **87**, 1625 (1987).
[28]W. G. Mallard, F. Westley, J. T. Herron, and R. F. Hampson, NIST Chemical Kinetics Database—Ver. 6.0, NIST Standard Reference Data, Gaithersburg, MD (1994).
[29]I. Nadler and S. Rosenwaks, J. Chem. Phys. **83**, 3932 (1985).
[30]Y. Ikezoe, S. Matsuoka, M. Takebe, and A. Viggiano, *Gas Phase Ion-Molecule Reaction Rate Coefficients Through 1986* (Mass Spectroscopy Society of Japan, Tokyo, 1987).
[31]E. W. Ellis, R. Y. Pai, E. A. Mason, and L. A. Viehland, At. Data Nucl. Data Tables **17**, 177 (1976).